




RESEARCH ARTICLE | AUGUST 25 2023

## Cohesive granular columns collapsing: Numerics questioning failure, cohesion, and friction

Lydie Staron  ; Laurent Duchemin; Pierre-Yves Lagrée 

 Check for updates

*J. Rheol.* 67, 1061–1072 (2023)  
<https://doi.org/10.1122/8.0000674>

  
View  
Online

  
Export  
Citation

CrossMark

### Related Content

Rheology and microstructure of unsaturated wet granular materials: Experiments and simulations

*Journal of Rheology* (September 2018)

Compliance of SLAC's laser safety program with the SLAC control of hazardous energy (COHE) program  
ILSC

Cohesion and aggregates in unsaturated wet granular flows down a rough incline

*Journal of Rheology* (June 2023)



**True powder rheology**

 **Anton Paar**

[Find out more](#)



# Cohesive granular columns collapsing: Numerics questioning failure, cohesion, and friction

Lydie Staron,<sup>1,a)</sup> Laurent Duchemin,<sup>2</sup> and Pierre-Yves Lagrée<sup>1</sup>

<sup>1</sup>*Sorbonne Université, CNRS—UMR 7190, Institut d'Alembert, F-75005 Paris, France*

<sup>2</sup>*ESPCI Paris, UMR 7636—Physique et Mécanique des Milieux Hétérogènes, F-75005 Paris, France*

(Received 14 April 2023; final revision received 4 July 2023; published 25 August 2023)

## Abstract

Simulations of the failure of cohesive granular steps with varying intensities of the contact adhesive force are presented. The simulations are compared with experimental and numerical studies of wet shear flows [Badetti *et al.*, *J. Rheol.* **62**, 1175–1196 (2018) and Khamseh *et al.*, *Phys. Rev. E* **92**, 022201 (2015)], computing the apparent friction coefficient. We observe consistent behaviors. We reproduce the dependence between the macroscopic cohesion and the contact adhesion [Rumpf, *Chem. Ing. Tech.* **42**, 538–540 (1970) and Richefeu *et al.*, *Phys. Rev. E* **73**(5), 051304 (2006)] observed experimentally for sticky polymer-coated grains, as well as the range of friction explored [Gans *et al.*, *Phys. Rev. E* **101**, 032904 (2020)]. Focusing on the interface between moving and static materials, and assuming a linear failure, we infer the orientation of the failure plane with the horizontal. We disclose a nonmonotonous evolution with the intensity of the contact adhesion. Assuming an ideal Coulomb material allows for proposing an interpretation to this nonmonotonous behavior. Although the systems are past incipient failure, we consider an edge of material at equilibrium, for which the failure angle is related to the internal frictional properties of the material. In this framework, the nonmonotonous evolution of the failure orientation may hint at a cohesion-induced weakening mechanism, by which stronger contact adhesion involve weaker friction. © 2023 The Society of Rheology. <https://doi.org/10.1122/8.0000674>

## I. INTRODUCTION

One enduring difficulty in describing the behavior of granular media lies in their ability to adapt external forcing by changing behavior, from flowing like a gas to resisting shear like a solid [1]. Adding adhesion between the grains further obscures the picture: clogging in flows and size-dependent stability threshold mix up with effective viscosity and material properties in a way still to be clarified. Because cohesive granular materials are causing many problems in manufacturing techniques, significant work has been carried out in the engineering community to describe the various behaviors of cohesive material and characterize their properties [2–10]. Powders are mostly involved, namely, very fine grains for which strong contact adhesion stems essentially from van der Waals forces. More academic considerations have also prompted numerous works [11–14]. The requirement for measurable well-constrained quantities often means using larger grains sticking together through capillary forces, which implies that weaker adhesive forces are accessible. Recently, the trade-off between cohesion control and cohesion strength has been mitigated by the design of sticky polymeric coating, thus opening the way to more quantitative measurements at both low and high contact adhesions and covering a large interval of macroscopic cohesion [15].

In this context, discrete numerical simulations can be of great help. Adding adhesive forces in the simulation contact

model actually leads to an unexpected outcome. Remarkably, Mandal *et al.* [16], applying a smooth Discrete Element Method (DEM) approach, uncovered the role of the contact stiffness and restitution in the cohesive behavior of the granular matter. Therefore, they stress the need for the definition of an effective cohesion, in which contact adhesion does not play the sole part [16]. In the same line, nonsmooth Contact Dynamics (CD) simulations show that the effective cohesion of granular samples increases with the mean duration of the contacts, embedded in the computational time step, which reflects the nonsmooth nature of the contact phenomena [17,18].

Consistent simulations allow for probing systems behavior over a large range of parameters; for instance, the effect of contact adhesion on the macroscopic cohesive properties of the material can be explored [11–13,19–23]. This allows for discussing the initial theoretical model of Rumpf [2], revisited in Richefeu *et al.* [11], predicting a linear relation between the cohesive strength, the structure of the packing, and the contact adhesive force.

Studying the structure of the packing is made easier by numerical approaches, giving access to the details of the packing arrangements, showing an increase of the density of contacts with adhesion strength and a decrease of the solid fraction [12,19,20,23,24]. The latter coincides with a strong expansion of the material and the emergence of stabilized loose structures when contact adhesion becomes large compared to the system average pressure [24,25].

The apparent friction  $\mu^*$  of the material can also be computed, showing consistently an increase of  $\mu^*$  with the macroscopic cohesion [13,20,24,25]. The study of Iordanoff *et al.*

<sup>a)</sup> Author to whom correspondence should be addressed; electronic mail: [lydie.staron@sorbonne-universite.fr](mailto:lydie.staron@sorbonne-universite.fr)

[26] differs nevertheless: a nonmonotonous behavior, with a decrease following the increase was observed, for large values of the cohesion. On the experimental side, Gans *et al.* [15], who estimated the Coulomb friction, did not observe any significant variation of the latter with the contact adhesion.

Most works addressing the behavior of cohesive granular matter adopt a stationary, uniform configuration as annular or planar shear flow, simplifying the computation of mean averaged quantities over well-defined flow regimes. The configuration adopted in this study contrast with these conditions since we are interested here in the failure of cohesive columns, which implies neither a uniform nor a stationary flow.

Besides, while most works on granular columns, including the collapse of cohesive material, concentrate on the run-out behavior or the deposit shape after the collapse [27–32], the present work focuses on the first instant of the failure. Assuming the failure to be a straight line opens an interesting way to explore the internal friction properties of the system. Although the hypothesis of a straight failure is a crude assumption if considered in the light of geomaterial science [33], it is nevertheless consistent with the laboratory observation of the failure of model cohesive granular material [34], as well as continuum simulations [23,34].

In the following, we first discuss the choice of a failure criterion allowing for proposing a chronology of the instability and the identification of the signature of the failure plane. We then evaluate the effect of the strength of the contact adhesion on the failure orientation, observing a nonmonotonous behavior. Computing the stress state of the simulated columns, and considering the equilibrium of an ideal Coulomb material, allows for questioning the mean behavior of the granular matter in terms of internal friction. More specifically, we discuss the likeliness of a cohesion-induced weakening mechanism.

The numerical cohesive failures are presented in Sec. II; the contact dynamics method and setup are introduced in Sec. II A, while Sec. II B details the unfolding of a failure. The identification of a robust criterion for characterizing the failure event is discussed in Sec. III, and the effect of adhesion strength on failure properties is presented. The stress state of the columns is analyzed in Sec. IV, and a Coulomb equilibrium is considered in Sec. V. The hypothesis of an ideal Coulomb material is discussed in Sec. VI, together with the possibility of a weakening mechanism induced by cohesion. The results are summarized in Sec. VII.

## II. COHESIVE FAILURES

### A. Details of the simulations

#### 1. Simulation method

A contact dynamics algorithm was applied to simulate simple two-dimensional (2D) cohesive systems [17,35,36]. The grains are circular beads with a diameter randomly chosen in the interval  $[4 \times 10^{-3} \text{ m}; 6 \times 10^{-3} \text{ m}]$ , and a mean diameter  $d = 5 \times 10^{-3} \text{ m}$ , to prevent crystalline ordering. Each contact is made cohesive through the introduction of a negative (i.e., tensile) force threshold  $-F_c$  in the Signorini's

contact graph, which specifies the acceptable values for the contact normal force  $N$ . Either the distance  $\delta$  between the grains is strictly positive, corresponding to a gap, and the contact force  $N$  is zero. Either  $\delta = 0$ , implying a contact, and  $N$  can take any values such that  $N \geq -F_c$  compatible with the equations of dynamics. In addition, an Amontons–Coulomb friction law is implemented, involving the contact coefficient of friction  $\mu_c$ . The tangential force threshold is supplemented with the adhesive force threshold: sliding is permitted when the tangential force has reached  $\mu_c(N + F_c)$ . The microscopic coefficient of friction is not varied:  $\mu_c = 0.2$ . The grains also interact through inelastic collisions, with a coefficient of restitution set to zero. Their volumetric density is  $\rho = 0.1 \text{ kg m}^{-2}$ .

A comprehensive presentation of the CD method will be found in Radjai and Richefeu [17].

The adhesive force threshold  $F_c$  is given in number of grains mean weight through the introduction of a granular Bond number  $B_{og}$  [24,37],

$$F_c = B_{og} m_{ij} g, \quad (1)$$

with  $m_{ij} = 2(\frac{1}{m_i} + \frac{1}{m_j})^{-1}$ , and  $i$  and  $j$  are the two grains in contact. Hence, the cohesive properties of the simulated systems will be set by the choice of the Bond number  $B_{og} = F_c/mg$ , giving the maximum adhesive resistance of contacts comparing to grain weight, which seems a sensible option since the failure sole driving is gravity. It is, however, a mere description of the contact adhesion but neither a measurement nor an estimation of the macroscopic cohesive properties of the systems, which will be discussed in Sec. VI.

Unlike numerical works modeling wet cohesive granular flows and describing cohesion as the result of capillary bonds [11,13,20,25], we do not assume a specific mechanism to induce contact adhesion. In particular, we do not assume debonding or rupture distance for a cohesive contact to be lost. On the contrary, we assume an adhesive force to be short-ranged so that a cohesive contact is lost as soon as it opens. We simply make them sticky by allowing contact forces to exist in a tensile state. In that sense, our numerical systems are closer to the “controlled-cohesion granular material” of Gans *et al.* [15] than to the “wet granular material” of Richefeu *et al.* [11].

#### 2. Generation of initial states

The systems are generated by deposition under gravity of 5572 circular grains in a rectangular container. The grains are initially cohesionless with a weak contact friction  $\mu_c = 0.2$ , thus forming dense packing with a volume fraction of  $\phi \simeq 0.82$ . When the systems have reached an equilibrium and all the grains are at rest, large adhesive contact forces are applied in order to sinter the structure ( $B_{og} = 100$ , corresponding to a yielding height of roughly  $50d$ ).

When launching the collapse simulation, the right wall closing the container is removed, and the Bond number is set to the desired value ( $B_{og} \in [0, 60]$ ). The systems, thus, reach the specified state of cohesion by decreasing the adhesion at initially sintered contacts, rather than increasing the adhesion

at initially cohesionless contacts. In this way, we are ensuring that the failure is not induced by weaknesses in a contact network initially incompatible with cohesion.

The diameter of the grains is randomly chosen in the interval  $[4 \times 10^{-3} \text{ m}; 6 \times 10^{-3} \text{ m}]$ , with a mean diameter  $d = 5 \times 10^{-3} \text{ m}$ , to prevent crystalline ordering. The random function assigning the sequence of diameters allows for the generation of fundamentally different, independent initial states in terms of grains and contacts arrangement, yet with identical macroscopic dimensions.

Following this procedure, 11 initial states were generated, and 11 independent runs could be performed for each value of the cohesion studied, totaling 132 independent runs, and allowing for the estimation of error bars.

The systems are bounded on the left hand side by a rigid vertical wall (Fig. 1). The columns have an initial height  $H \simeq 45d$  and a width  $R \simeq 120d$ , namely, an aspect ratio  $a \simeq 0.37$ . This squat geometry allows for the generation of failures far enough from the left wall so that they remain unaffected by its presence.

## B. Unfolding of a failure

At initial time  $t = 0$ , the right-hand-side wall is removed, and the columns are left to fail and spread onto a horizontal plane made rough by gluing grains on it (Fig. 1). Because the present work is interested in the failure onset, and not on the ensuing spreading, we focus on the first instant of the evolution, recording the system state every  $\Delta t = 10^{-3} \text{ s}$ . The computational time step is  $dt = 2 \times 10^{-4} \text{ s}$ , coinciding with a mean grain overlap between  $3 \times 10^{-3}d$  (for  $B_{og} = 0$ ) and  $4 \times 10^{-3}d$  (for  $B_{og} = 60$ ).

The Bond number is successively set to  $B_{og} = 1, 2, 3, 4, 5, 10, 20, 30, 40, 50$  and  $60$ . In addition, the non-cohesive case  $B_{og} = 0$  is also considered.

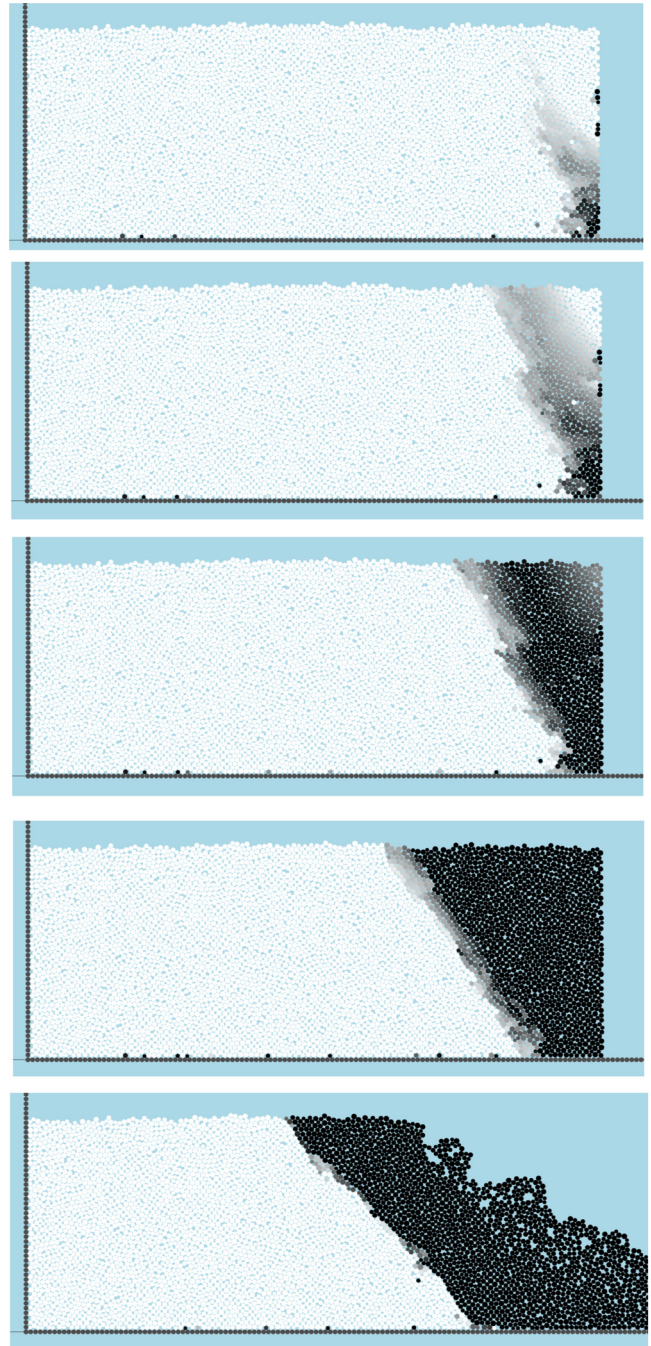
The column height  $H \simeq 45d$  of the system and the combination of contact adhesion explored coincide with unstable states as studied in Abramian *et al.* for similar systems [23]. If we suppose that the yielding height  $H_y$  satisfies  $H_y/d \simeq 0.5B_{ond}$ , as observed in [23], the systems studied here range from  $H/H_y \simeq 1.5$  for  $B_{og} = 60$  to  $H/H_y \simeq 8$  for  $B_{og} = 10$ . For smaller  $B_{og}$  numbers, the predicted yielding height is smaller than  $5d$ . In that finite-size limit, the definition of a yielding height itself, according to a continuum picture of the systems, is no longer straightforward.

Figure 1 shows an example of the early instant of a failure for  $B_{og} = 30$ . The present paper focuses on the analysis of system properties for failure evolution corresponding roughly to the first four pictures. They coincide with a quasistatic part of the systems evolution, with a mean velocity of the order of  $\sim 10^{-2} \sqrt{gH}$  (not shown).

The later stages of the evolution are nevertheless discussed in relation to the evolution of the stress tensor in Sec. IV.

## III. FAILURE CHARACTERIZATION

In this section, we give the details of the method applied to detect the occurrence of the failure both in space and time. Because one aim of the study is to quantify the effect of cohesion onto the failure characteristics, the criteria must



**FIG. 1.** Successive snapshots of the initiation of a failure in a cohesive granular step with a contact adhesion  $B_{og} = 30$ . The gray color scale shows the grain cumulative displacement in the interval  $[r_{th}; 1.4r_{th}]$ , where  $r_{th} = 0.1d$ . Time shown are, from top to bottom,  $t_1/T = 0.10$ ,  $t_2/T = 0.11$ ,  $t_3/T = 0.12$ ,  $t_4/T = 0.17$ , and  $t_\infty/T = \infty$ ,  $T = \sqrt{H/g} = 0.1515 \text{ s}$ .

be valid and must carry the same information for any intensity of the contact adhesion. We explain here how this is achieved.

### A. Defining a displacement threshold

A simple way of characterizing the occurrence of a failure in a system of a few thousands grains is to track the displacement of the grains, without presuming the location of the

displacement, nor its orientation. To this end, one needs to define a displacement threshold to separate those grains that have moved from those that will be considered static, considering that very small rearrangements in the bulk coexist with larger failure-induced motions [36].

For illustration, we show the behavior of the simulation series with a contact adhesion  $B_{og} = 30$  for three values of the displacement threshold  $r_{th}$ . We consider  $r_{th} = 0.05d$ ,  $r_{th} = 0.20d$ , and  $r_{th} = 0.50d$ . We denote  $\Delta r_i$  the cumulative displacement of each grain  $i$ . For each value of  $r_{th}$ , the number of grains  $N_{th}$  whose cumulative displacement  $\Delta r_i$  exceeds  $r_{th}$  is measured. The behavior of  $N_{th}$  with time is displayed for  $B_{og} = 30$  in Fig. 2, averaged over 11 independent runs; the error bars show the corresponding standard deviation.

We observe, in each case, a sharp steplike evolution, with a distinct quick increase, which we identify as the onset of stability loss and the occurrence of a failure. A rapid saturation follows, which coincides with the flow of detached material running away with no significant number of additional grains further displaced beyond the value of the threshold.

Small values of  $r_{th}$  also probe diffuse motion of grains in the bulk and induce large error bars. On the contrary, error bars nearly vanish for large displacement threshold. Yet focusing on large values of  $r_{th}$  also means that you miss out the early stages of the failure, with a risk of probing the erosion induced by the failure, rather than the failure itself.

To elect a value of  $r_{th}$  allowing for discriminating between diffusionlike motion and failure-induced motion, the distribution of displacements  $f$  over the time interval  $[0, T]$  is considered. We compute the number of grains displaced in intervals  $[r_{th}, r_{th} + 0.001d]$ , normalized by the total number of grains:  $f(r_{th}) = \delta N_{th}/N_p = (N_{th}(r_{th} + 10^{-3}d) - N_{th}(r_{th}))/N_p$  for  $r_{th}$  varying between  $[0, 5d]$ . The outcome for a small value of contact adhesion  $B_{og} = 2$  is plotted in Fig. 3.

We observe that a Gaussian behavior is an acceptable approximation up to  $r_{th}/d \simeq 0.07$ , bespeaking a diffusionlike dynamics. Beyond  $r_{th}/d \simeq 0.07$ , the distribution deviates from a Gaussian trend: additional small motions, presumably

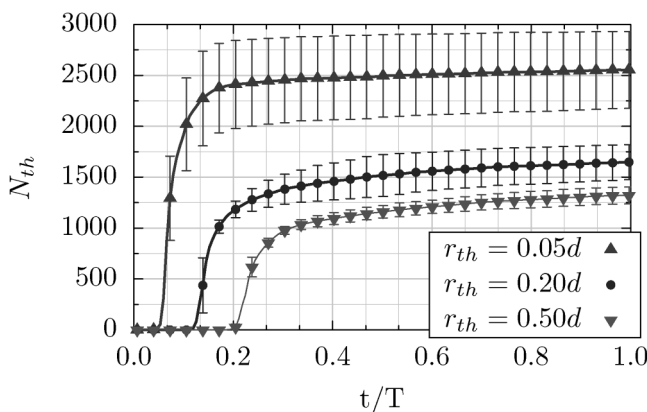


**FIG. 2.** Number of grains  $N_{th}$  whose cumulative displacement exceeds the displacement threshold  $r_{th}$  in the course of time, for three values of  $r_{th}$ , for a contact adhesion  $B_{og} = 30$ . The error bars show the corresponding standard deviation computed over 11 runs.

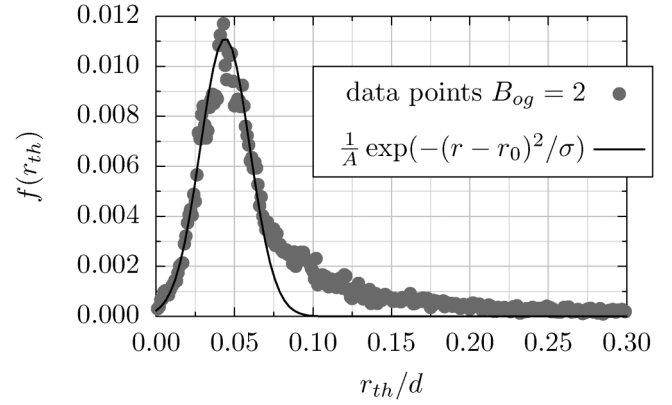


**FIG. 3.** Distribution of displacements over a time interval  $[0, T]$ , as a function of the displacement value  $r_{th}$ , and the Gaussian approximation with  $A = 90$ ,  $r_0/d = 0.044$ , and  $\sigma = 0.1$ ; for  $B_{og} = 2$ .

induced by the failure, contribute to the distribution. From  $r_{th}/d \simeq 0.1$  onward, the Gaussian function vanishing suggests that small diffuse motion in this domain is caused by the failure dynamics only. In the following, to make sure that we do filter out all diffuse motion in the system, we chose twice this value to characterize the failure, namely,  $r_{th}/d = 0.2$ . Because more intense contact adhesion tends to shift the distribution toward smaller displacements, the threshold value  $r_{th}/d = 0.2$  is also adequate for larger values of the Bond number.

## B. Identifying the failure chronology

The smooth evolution of  $N_{th}$  with time allows for the identification of the onset of the stability loss, but not exactly the occurrence of a well-defined failure.

A natural choice is to detect an inflection point in the evolution of  $N_{th}$ , simply plotting

$$\Delta N_{th} = N_{th}(t + \Delta t) - N_{th}(t) \quad (2)$$

as a function of time, namely, the instantaneous number of grains passing the displacement threshold  $r_{th}$  ( $\Delta t = 1.10^{-3}$ ).

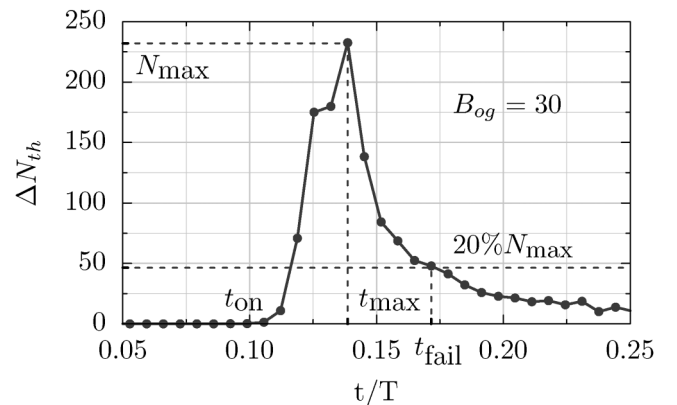


**FIG. 4.** Variations of the number of grains having overpassed the displacement threshold  $r_{th} = 0.20d$  in the course of time, in the case of a contact adhesion  $B_{og} = 30$ . The onset time  $t_{on}$ , the peak time  $t_{max}$ , and the estimated failure time  $t_{fail}$  are also shown ( $T = \sqrt{H/g}$ ).

For illustration, the first moments of the evolution of  $\Delta N_{\text{th}}$  for  $r_{\text{th}} = 0.20d$  and a contact adhesion  $B_{og} = 30$  are plotted in Fig. 4. A peak value—corresponding to the inflexion point—clearly comes out, after a rapid ascent bringing an increasing number of grains beyond the displacement threshold. A slower descent follows, corresponding to more localized motion involving fewer and fewer newly mobilized grains.

We define the time  $t_{\text{on}}$  at which motion onset is detected ( $\Delta N_{\text{th}} > 0$ ) and the time  $t_{\text{max}}$  at which the peak (maximum) value  $N_{\text{max}}$  is reached. Both  $t_{\text{on}}$  and  $t_{\text{max}}$  are specific for each simulation. We find that they take well-defined values for each cohesion intensity; for instance,  $t_{\text{on}}/T \simeq (0.111 \pm 8\%)$  and  $t_{\text{max}}/T \simeq (0.140 \pm 5\%)$  for  $B_{og} = 30$ .

Singling out the best instant to characterize the failure occurrence is, however, difficult. The instant  $t_{\text{max}}$  of the peak value seems an obvious candidate. However,  $t_{\text{max}}$  coincides with an early state where a modest number of grains is mobilized. Moreover, it does not offer a well-defined reproducible pattern for all values of the cohesion.

Hence, we prefer to focus on a later stage of the evolution when the failure has somewhat settled, and the number of newly mobilized grains has fallen from 80% of its maximum value. We denote the corresponding time  $t_{\text{fail}}$ . For the example case  $B_{og} = 30$ , we find  $t_{\text{fail}}/T \simeq 0.157 \pm 5.7\%$ . The graph in Fig. 4 may give the feeling that  $t_{\text{fail}}$  is already at the end tail of the failure process; certainly, some grains mobilized at  $t_{\text{fail}}$  are responding to the beginning of the propagation of the failure rather than being a picture of its onset. However, plotting  $\Delta N_{\text{th}}$  against the evolution of the mean grain velocity  $\langle V \rangle / \sqrt{gd}$  shows that  $t_{\text{fail}}$  is still in the very first stage of the failure (not displayed). This can also be inferred from Fig. 1, showing that the time interval in which  $t_{\text{fail}}$  falls (between  $t_3$  and  $t_4$ ) corresponds to imperceptible system deformations to the naked eye. Hence, we do not expect the effect of failure propagation to be dominating.

### C. Failure geometry

We now consider the position of the grains whose cumulative displacement  $\Delta r_i$  exceeds the threshold value  $\Delta r_i \geq r_{\text{th}}$  at time  $t_{\text{fail}}$ . We then focus on the position of the grains at the interface between mobilized grains ( $\Delta r_i \geq r_{\text{th}}$ ) and static grains ( $\Delta r_i < r_{\text{th}}$ ) and consider that this interface forms a correct proxy of the shape of the failure.

An example is given in Fig. 5 for the system displayed in Fig. 1. We observe that the interface can be approximated by a straight line, the slope of which gives an estimation of the failure orientation  $\alpha$  with the horizontal. The assumption of a linear failure is certainly in contradiction with the observation of geomaterials behavior [33,38]; yet, it is consistent with an experimental observation of cohesive granular failure. The cohesive granular material simulated in this work has no claim to resemble geomaterials. Straight lines being a quite convenient geometry to confront hypothesis, assuming linear failures seem a reasonable option.

The slope of the interface in Fig. 5(b) is  $-1.90$ , with a regression standard error of 2.3%. Figure 5(c) shows the position of the grains displaced in the interval  $[r_{\text{th}}, r_{\text{th}}(1 + 15\%)]$  at time  $t_{\text{fail}}$  for the same simulation, confirming that the

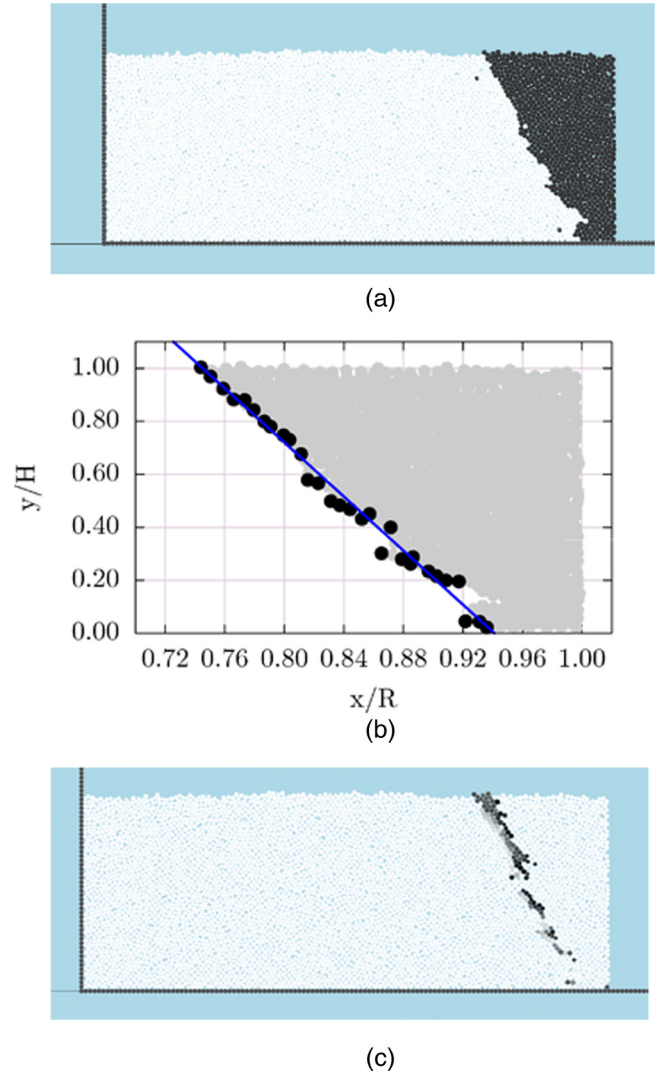


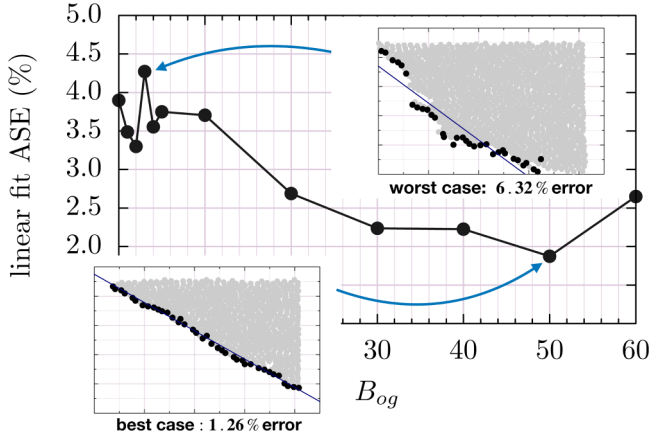
**FIG. 5.** (a) Position of the grains whose cumulative displacement  $\Delta r_i$  exceeds the threshold value  $r_{\text{th}}$  at time  $t_{\text{fail}}$ :  $\Delta r_i \geq r_{\text{th}}$  (in black), (b) the corresponding linear regression of the interface between static and mobilized region defining the failure orientation, and (c) the position of the grains displaced in the interval  $[r_{\text{th}}, r_{\text{th}}(1 + 15\%)]$  at time  $t_{\text{fail}}$  (gray shade).

interface between mobilized and static grains is a reliable signature of the failure geometry.

This analysis, discriminating between mobile and static grains applying displacement binary criteria, resembles the outcome from image correlation technics. The latter, used in [34,39,40], reveal linear failure in collapsing cohesive columns. Continuum simulation of cohesive granular failures also reveal linear failure geometry in [32,34].

### D. Quality of the linear approximation

Contact adhesion changes the morphology of the failures. The shear band associated with small values of contact adhesion is wider and less localized than those associated with larger contact adhesion. As a result, the linear approximation of the static/mobile interface shows larger standard error in the regression procedure for smaller contact adhesion (not to be mixed with the standard deviation measured from the set of values of  $\alpha$  in each  $B_{og}$  simulation series). This can be seen in



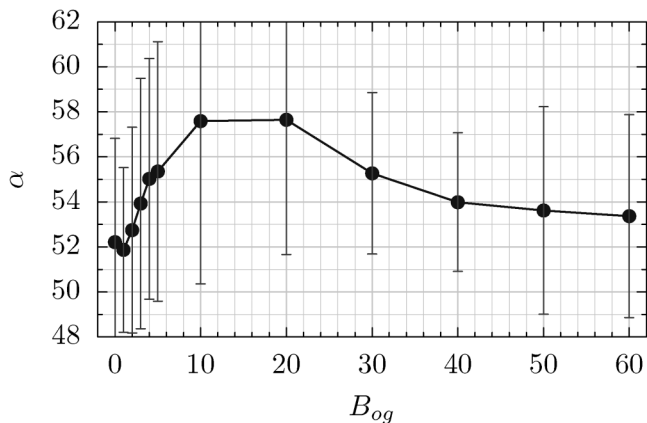
**FIG. 6.** Mean asymptotic standard error (ASE) of the linear approximation of the static/mobile interface as a function of contact adhesion  $B_{og}$ . The best case (error of 1.26% with  $B_{og} = 50$ ) and the worst case (error of 6.32% with  $B_{og} = 3$ ) taken from all 132 simulations are shown for illustration.

Fig. 6, where the averaged asymptotic standard error (ASE) associated with the regression process in each simulation series is plotted against the value of the contact adhesion.

Figure 6 also shows the worst and best case scenario from all 132 simulations. The worst case scenario (from simulation series with  $B_{og} = 3$ ) exhibits a linear approximation with a rather poor performance, yet not typical. Indeed, the associated error (6.32%) definitely overpasses the mean ASE for the set of simulations with  $B_{og} = 3$ , which is 4.27%, and by far the mean ASE for all the weak adhesion interval  $B_{og} \in [0:10]$ , which is 3.71%. The best case scenario on the contrary exhibits a very neat line, which is more representative of the adhesion interval  $B_{og} \in [20:60]$ , if not strictly typical. Indeed, the associated error (1.26%) stands out less in this interval, which exhibits a mean ASE of 2.33%.

### E. Cohesion and failure slope

Following the steps described above, we analyze all 11 independent simulations in each of the 12 simulations series in the adhesion interval  $B_{og} \in [0:60]$ . For each run, we estimate the orientation of the failure with the horizontal  $\alpha$ . We



**FIG. 7.** Failure orientation with the horizontal  $\alpha$  as a function of the contact adhesion Bond number  $B_{og}$ . The error bars show the corresponding standard deviation.

also compute the corresponding standard deviation in each simulation series. The outcome is displayed in Fig. 7.

The first comment is that the error bars are large, showing the dispersion of the data. This is not a completely surprising fact for dry granular matter, for which static angles of repose, or avalanche size measured as the hysteresis angle, also exhibit comparably large dispersion [41]. A second comment is that the amplitude of the contact adhesion seems to have no noticeable effect on the dispersion of the results, although it does affect positively the linear approximation of the failure (see Subsection III D).

The nonmonotonous behavior seems nevertheless a well-defined feature, with the slope of the failure increasing with contact adhesion for smaller values of the latter, but decreasing for stronger contact adhesion. In the following, we will discuss these results in terms of the frictional properties of the material, computing the apparent friction and considering a Mohr–Coulomb approach of cohesive granular media.

## IV. COMPUTING THE APPARENT FRICTION

The failure and collapse of unconfined granular columns are strongly nonuniform and nonstationary events. This significantly affects the evolution of the stress state of the systems, as discussed in what follows.

### A. The stress tensor

Stresses are computed following the classical micromechanical definition, including forces transmitted both by long-lasting contact interactions, and short-lived collisions induced by velocity fluctuations [20]. These two contributions, quantified by the static stress tensor  $\sigma^s$  and the kinetic stress tensor  $\sigma^k$ , form the total stress tensor  $\sigma$ ,

$$\sigma = \sigma^s + \sigma^k, \quad (3)$$

$$\sigma = \frac{1}{V} \sum_{c \in N_c} \mathbf{f}^c \otimes \mathbf{r}^c + \frac{1}{V} \sum_{p \in N_p} m_p \delta \mathbf{v}^p \otimes \delta \mathbf{v}^p, \quad (4)$$

where  $\mathbf{f}^c$  is the force transmitted by the contact  $c$  and  $\mathbf{r}^c$  is the center-to-center vector,  $m_p$  is the mass,  $\delta \mathbf{v}^p$  is the velocity fluctuation of grain  $p$ ,  $N_c$  and  $N_p$  are the number of contacts and grains, respectively, over which the summation is made,  $V$  is the volume over which the stress is computed, and  $\otimes$  is the dyadic product.

Figure 8 shows the pressure computed for each stress tensor  $\sigma^s$ ,  $\sigma^k$ , and  $\sigma$ , computed as the sum of the eigenvalues of each tensor, and denoted, respectively,  $P^s$ ,  $P^k$ , and  $P$ . The case  $B_{og} = 30$  is chosen here for illustration. We observe a sudden jump of the static pressure  $P^s$  at the start of the simulation. This coincides with the sudden loss of cohesive contacts and the emergence of newly formed contact following the removal of the right-hand-side wall. We also see that the kinetic pressure  $P^k$  has a weaker contribution. It becomes, however, non-negligible when  $0.5 \lesssim t/T$ , coinciding with the more dynamical part of the failure, when the pile starts collapsing. As a result, the total pressure  $P$  is dominated by the static stress in the first instant of the simulation, being equal

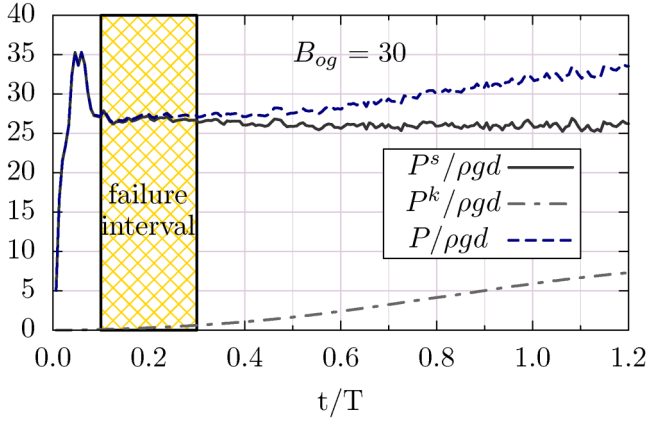


**FIG. 8.** Time evolution of pressure  $P^s$ ,  $P^k$ , and  $P$  computed from the static, kinetic, and total stress tensors  $\sigma^s$ ,  $\sigma^k$ , and  $\sigma$ , here averaged on the simulation series with  $B_{og} = 30$ . The shaded area shows the failure time interval (see the text).

or similar to  $P^s$ , but starts reflecting the kinetic stress as the material fails, at a later stage.

These features are shared by all simulations for any intensity of contact adhesion. However, the stronger the adhesion, the less significant the kinetic stress. Figure 9 shows the ratio of the static pressure  $P^s$  to the total pressure  $P$  as a function of  $B_{og}$ , averaged over two different time intervals. The first interval  $t/T \in [0:1.3]$ , or the “collapse interval,” spans the whole duration of the simulations, from the failure to the start of the spreading of the detached material. The second interval  $t/T \in [0.1:0.3]$ , or the “failure interval” (shown in Fig. 8), is focusing on the early instant of the failure, when the evolution is essentially quasistatic. We observe for both interval how adhesion favors the contribution of the static stress to the total stress state, with  $P^s/P$  increasing with  $B_{og}$ . More to the point, we see that the stress state is largely dominated by the static stress in the failure interval  $t/T \in [0.1:0.3]$ , where velocities, and, thus, kinetic stresses, are nearly zero. In the following, we will consider this failure

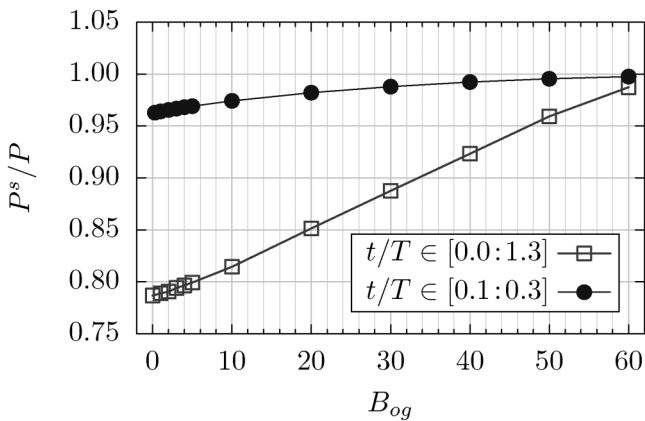


**FIG. 9.** Ratio of the pressure  $P^s$  measured by the static stress tensor  $\sigma^s$  to the total pressure  $P$  measured by the total stress tensor  $\sigma$ , evaluated over different time intervals. The static stress tensor is consistently dominating the total stress in the failure interval  $t/T \in [0.1:0.3]$ , during which the evolution is quasistatic or very slow ( $P^s/P > 95\%$ ). We observe that strong adhesive forces favor the contribution of the static tensor, with the ratio  $P^s/P$  increasing with  $B_{og}$  in both time intervals.

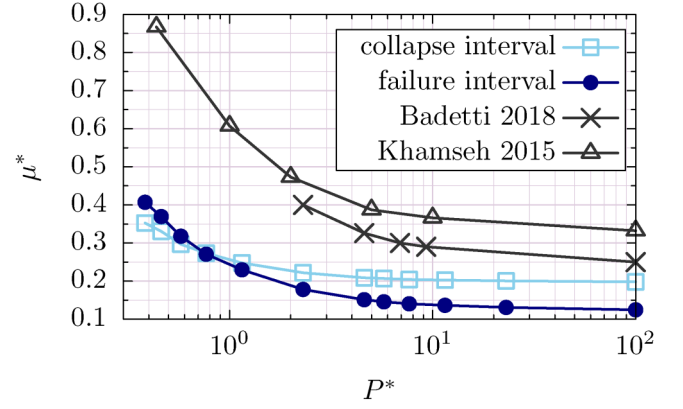


**FIG. 10.** Apparent friction  $\mu^*$  computed in the failure time interval  $t/T \in [0.1:0.3]$  and in the collapse time interval  $t/T \in [0:1.3]$ , as a function of the reduced pressure  $P^*$ . The data from [13,20] are also reproduced.

interval  $t/T \in [0.1:0.3]$  to evaluate the apparent friction associated with the failure onset.

## B. The apparent friction $\mu^*$

The apparent friction  $\mu^*$  is defined as the ratio of the deviatoric stress  $Q$  to the pressure  $P$ , both computed as functions of the eigenvalues of the total stress tensor  $\sigma$ :  $\mu^* = Q/P$ . Figure 10 shows the apparent friction  $\mu^*$  measured and/or computed for sheared samples of wet granular matter as a function of the reduced pressure  $P^*$  in Khamseh *et al.* [20] and in Badetti *et al.* [13] (see<sup>1</sup> for details). The reduced pressure is defined as the ratio of the system characteristic pressure (or normal confining stress) and the characteristic adhesive stress, namely, comparing the cohesion with the mean stress level of the system [13,20]. In the simulations discussed here, presenting unconfined failures, the only pressure stems from gravity. We, thus, define the reduced pressure  $P^*$  as the ratio of the gravity-induced pressure seen by the center of mass of the packing  $\frac{1}{2}\rho\phi gH$  (where  $\phi$  is the solid fraction) divided by the contact adhesive stress  $F_c/d$ , thus giving  $P^* = (2\phi H)/(\pi d B_{og}) \simeq 23/B_{og}$ .

The simulation apparent friction  $\mu^*$ , computed over the failure time interval  $t/T \in [0.1:0.3]$ , is displayed in Fig. 10 together with the data from [13,20]. Note that we have artificially defined  $P^* = 100$  for  $B_{og} = 0$ , in order to allow for comparison with the very low cohesion data from [13,20]. The behaviors are very comparable in terms of dependence on  $P^*$ , exhibiting a marked increase with  $1/P^*$ . However, the values of  $\mu^*$  of the simulations are much weaker, with  $\mu^* \simeq 0.125$  for  $P^* \rightarrow \infty$  and  $\mu^* \simeq 0.4$  for  $P^* \rightarrow 0$ , instead of 0.33 and 0.87 observed by [20], for instance.

One may invoke a difference of contact friction, set to  $\mu_c = 0.2$  in the present simulations. However, the data from [13,20], using, respectively,  $\mu_c = 0.3$  and  $\mu_c = 0.09$ , both coincide with a larger apparent friction. Hence, the value of the contact friction does not provide any explanation.

<sup>1</sup>Data extracted from Table 1 in [20] and from Fig. 7 in [13].



Another source of discrepancy could be the flow regime in which the apparent friction is measured. While Khamseh *et al.* [20] and Badetti *et al.* [13] are considering flowing material under shear, the stress state of the simulations presented here is essentially measured over a static state. However, the flow inertial number  $I$  investigated in [13,20] spans a large interval, including very small values:  $I \in [10^{-4}, 5 \cdot 10^{-1}]$ , showing continuity of behavior so that the gap between static and flowing regimes is bridged.

Interestingly though, in the present simulations, the apparent friction becomes larger when computed over the collapse interval  $t/T \in [0; 1.3]$ , where the contribution of the kinetic stress becomes non-negligible (plotted in Fig. 10). This is consistent with the observation of friction increasing with the inertial number for dry granular matter [42]. In our case, considering the collapse interval where the kinetic contribution is non-negligible, brings the apparent friction  $P^* \rightarrow \infty$  from  $\mu^* = 0.125$  to  $\mu^* \simeq 0.2$ . This latter figure is consistent with the deposit slope of  $\sim 11.5^\circ$  after the system has spread.

More relevant to friction might be the contact model chosen for simulating the granular media. Independently of the algorithm differences in CD and DEM methods, [13,20] are considered wet systems, where adhesive forces are capillary bridges. An essential feature of this type of adhesive interactions is the introduction of a debonding (or rupture) distance, at which the attractive force vanishes. The existence and extension of this debonding distance were shown to play a significant role in the value of the apparent friction [20]. By contrast, our cohesive samples are simple sticky beads, with short-ranged adhesion, for which attractive forces vanish as soon as contact is lost. In that sense, our systems resemble more the cohesion-controlled granular material designed by Gans *et al.*, for which no capillary bonds were observed [15]. Consistently, the present numerical observations are closer to the variations of friction with the contact adhesion observed experimentally by Gans *et al.*, spanning a range of friction between 0.2 and 0.5 for a  $B_{og}$  varying between 5 and 50.<sup>2</sup>

## V. A COULOMB EQUILIBRIUM MODEL

Assuming the cohesive granular systems to be an ideal Coulomb material gives us means of questioning the failure orientation  $\alpha$  in terms of the material internal friction angle [43].

We consider a simplified equilibrium configuration along a linear failure following [23,34,44]. Although this geometry does not render the complexity of geotechnical observations, it reproduces experimental and numerical observations for model granular matter [34,36].

We suppose the equilibrium of the material along a failure plane of length  $\ell$ , oriented at an angle  $\alpha$  with the horizontal, as illustrated in Fig. 11. Assuming that the shear stress  $\tau$  and the normal stress  $\sigma_n$  satisfy the Mohr–Coulomb model, introducing a macroscopic cohesion  $\tau_c$ , and a coefficient of internal friction  $\mu$ , the equilibrium of the upper corner is

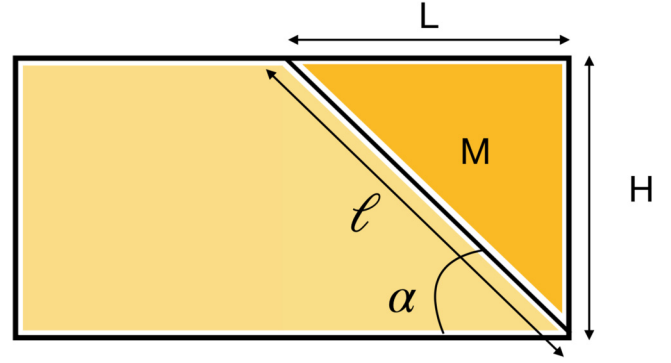


FIG. 11. Stability of a cohesive granular step: slip motion of a corner of mass  $M$  along the failure plane at incipient failure.  $L$  and  $H$  are, respectively, the horizontal extent of the failing corner and the height of the step;  $\ell$  is the length of the failure plane and  $\alpha$  its orientation horizontally.

compromised when

$$\tau = \mu\sigma_n + \tau_c, \quad (5)$$

leading to

$$Mg \sin \alpha = \mu Mg \cos \alpha + \tau_c \ell, \quad (6)$$

where  $M$  is the mass of the failing part [23,34,44]. Denoting  $H$  the height of the step and  $\rho$  the density of the material, we have  $M = \frac{1}{2}\rho H^2 / \tan \alpha$  and  $\ell = H / \sin \alpha$ . Equation (6) can readily be written in the form

$$H = \frac{2\tau_c}{\rho g} \frac{1}{(\cos \alpha \sin \alpha - \mu \cos^2 \alpha)}, \quad (7)$$

which, considering the internal angle of friction  $\varphi$  such that  $\mu = \tan \varphi$ , becomes

$$H = \frac{2\tau_c}{\rho g} \frac{\cos \varphi}{\cos \alpha \sin(\alpha - \varphi)}. \quad (8)$$

The minimum height  $H_y$  of a failing step, namely, a system just passed the equilibrium, is, thus, given by minimizing the function  $1 / \cos \alpha \sin(\alpha - \varphi)$ . The latter have a minimum at  $\cos(2\alpha - \varphi) = 0$ , and the failure orientation of a system of height  $H_y$  satisfies  $\alpha = \pi/4 + \varphi/2$ . Conversely, the friction angle is given by  $\varphi = 2(\alpha - \pi/4)$ .

If the simulations were close to equilibrium, namely,  $H \simeq H_y$ , the evolution of the failure orientation with cohesion in Fig. 7 could be interpreted in terms of frictional properties. The coefficient of internal friction can be estimated as  $\mu = \tan \varphi$ , with Eq. (8) leading to  $\varphi = 2(\alpha - \pi/4)$  at  $H \simeq H_y$ . The outcome for the numerical failures is plotted in Fig. 12, together with the data from [13,20]. While  $\varphi = 2(\alpha - \pi/4)$  increases with the strength of contact adhesion at small values of  $B_{og}$ , following the evolution of the failure orientation, a weakening mechanism would appear at larger  $B_{og}$  values, with friction slowly decreasing with increasing adhesion strength. Since stronger adhesive forces at contact between grains signify a more solidlike interface

<sup>2</sup>Data extracted from Fig. 14 in [15].

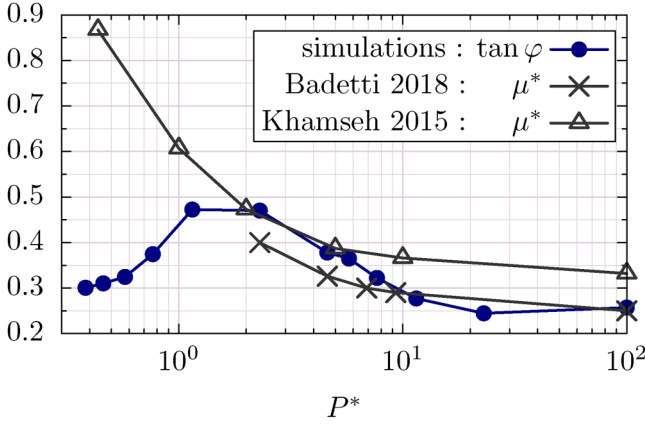


FIG. 12. Friction coefficient as a function of the reduced pressure  $P^*$  defined as  $\mu = \tan \varphi$  for the simulations and as  $\mu^* = \tau/\sigma_n$  for the experimental and numerical data from [13,20].

between two sliding blocks at failure, and less erratic dissipative collisions, stronger cohesion resulting in smaller friction seems a sensible scenario.

The decrease of friction properties with cohesion was (to our knowledge) only reported in a numerical study of the flow of the third body in Jordanoff *et al.* [26], considering plane shearing and intense values of contact adhesion. By contrast, apparent friction increasing with cohesion is consistently observed experimentally and numerically [13,20,24].

However, applying  $\varphi = 2(\alpha - \pi/4)$ , which is a result stemming from stability analysis when the yielding height  $H_y$  is just reached, is not a straightforward valid operation for our systems. Indeed, their height  $H$  is well above  $H_y$  for all values of  $B_{og}$  studied here (see Sec. II B). In addition,  $\alpha$  was shown to vary with the height of the systems [34,40,45]. Hence,  $\alpha(H > H_y)$  is not equivalent to  $\alpha(H \simeq H_y)$  in terms of failure orientation, hence in terms of friction. Drawing definite conclusion on the frictional properties from the behavior of  $\alpha$  with  $B_{og}$  is, thus, not possible here.

## VI. AN IDEAL COULOMB MATERIAL?

The equilibrium analysis performed above relies on the assumption that the cohesive granular material is an ideal Coulomb material, satisfying, at incipient slip, the simple relation between shear stress  $\tau$ , normal stress  $\sigma_n$ , internal friction  $\mu$ , and cohesion  $\tau_c$  [43],

$$\tau = \mu\sigma_n + \tau_c. \quad (9)$$

The value of the macroscopic cohesion  $\tau_c$  is not straightforward to estimate. For both experimental and numerical studies,  $\tau_c$  is often derived from series of measurements of  $(\tau, \sigma_n)$  for flows with a given cohesion; the locus of the affine approximation of the resulting set of points provides an estimate of  $\tau_c$  [5,6,11,15]. Such a measurement is not feasible in the present collapse configuration.

We can, however, aim at an estimation of  $\tau_c$  based on a theoretical prediction proposed in Richefeu *et al.* [11] and developed for 2D systems in Abramian *et al.* [23].

The analysis developed by Richefeu *et al.* [11] from the Rumpf equation [2] relates the value of the tensile strength, in the absence of confining pressure, to the contact adhesive interactions, and the structure of the packing, for 3D wet granular media. We apply the same reasoning, modifying it for 2D quasimonodisperse systems and using expression (1) for the contact adhesive force  $F_c$ , rather than capillary forces. Following [11], the density of cohesive contacts  $Z_c$  is given by half the mean number of cohesive contacts per particle, divided by the particle free volume in 2D (i.e., the average particle volume  $V_p = \pi d^2/4$  divided by the solid fraction  $\phi$ ),

$$\sigma_c = \frac{\phi Z_c}{\pi d} F_c, \quad (10)$$

with  $\phi$  being the packing volume fraction and  $Z_c$  the mean number of cohesive contacts per particle. Considering the contact adhesive forces  $F_c = mgB_{og} = \rho g V_p B_{og}$ , the theoretical prediction for the macroscopic cohesion of an assembly of cohesive particles  $\tau_c = \mu\sigma_c$  is given by

$$\tau_c = \frac{d}{4} \mu \phi Z_c \times \rho g \times B_{og}, \quad (11)$$

where  $\mu$  is the internal coefficient of friction.

Since the present simulations involve initial states prepared using zero friction to generate dense packings, sintered afterward using a large value of contact adhesion  $B_{og} = 100$ , all our systems present a large initial packing fraction  $\phi \simeq 0.82$ , which does not vary until the failure crack has developed. In the following, we will, thus, consider the constant value  $\phi = 0.82$ .

Estimating  $\tau_c$  also requires that we have an estimate for the internal friction  $\mu$ , different from the apparent friction  $\mu^*$  computed in Sec. IV. We simply set  $\mu = 0.3$ , which seems a reasonable value.

Finally, we need to estimate  $Z_c$ . Although any contact can withstand a tensile state, not all contact do exist in this peculiar state. In the following, we consider a contact to be cohesive if it actually carries a tensile force. The time evolution of  $Z_c$  for three values of  $B_{og}$ , corresponding to weak, medium, and strong contact adhesion, is shown in Fig. 13.

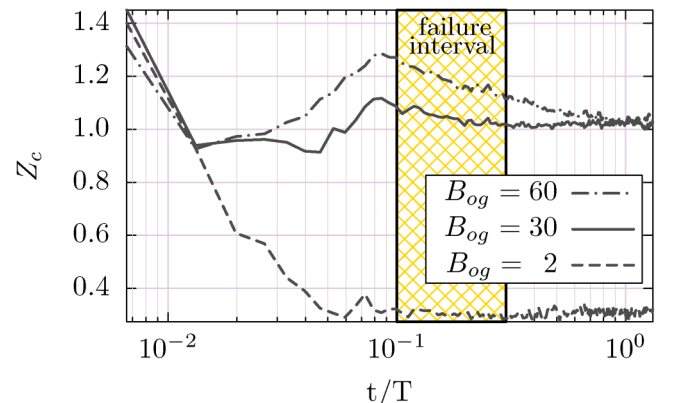
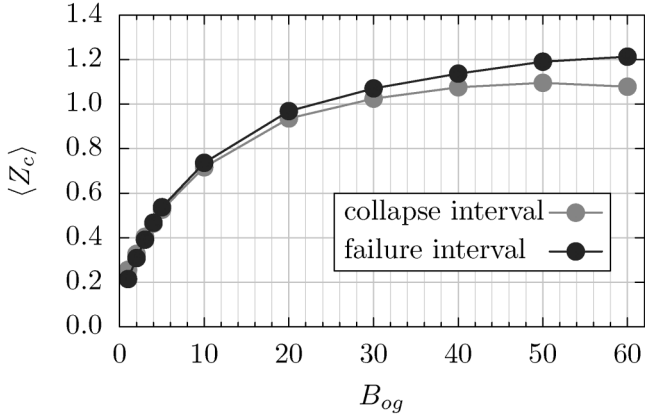


FIG. 13. Density of cohesive contacts  $Z_c$  as a function of time for three different values of contact adhesion  $B_{og}$ .



**FIG. 14.** Mean density of cohesive contacts  $\langle Z_c \rangle$  as a function of the contact adhesion  $B_{og}$  number, computed over the collapse time interval  $t/T \in [0;1.3]$  and the failure time interval  $t/T \in [0.1;0.3]$ .

Plotting  $Z_c$  as a function of  $B_{og}$ , averaged over either the collapse interval or the failure interval, shows how larger contact adhesion coincides with a larger density of cohesive contacts (displayed in Fig. 14):  $Z_c \simeq 0.3$  for  $B_{og} = 2$ , while  $Z_c \simeq 1.2$  for  $B_{og} = 60$ . For comparison, the mean number of contacts per particle (or “coordinance”) is around 3.5.

In a first try, we estimate the cohesive stress  $\tau_c$  considering the value of  $Z_c$  for each series of simulations independently, as they are given in Fig. 14 for the failure interval. The outcome of relation (11) is plotted Fig. 15. Expectedly, the plot reflects the behavior of  $Z_c(B_{og})$  in Fig. 14.

In a second try, following [11,15], we take a constant value for  $Z_c$ . We set  $Z_c = 1.2$ , corresponding to the case  $B_{og} = 60$ . The plot becomes linear, but with a lower proportionality constant than the prediction describing the experimental data from [15], due to the fact that we have not considered that all contacts are cohesive as in [11,15].

Eventually, if we consider that all contacts are cohesive following [11,15], equating  $Z_c$  with the grains mean coordination number  $Z_c = 3.5$ , the result of the simulations becomes very similar to that of Gans *et al.* [15].

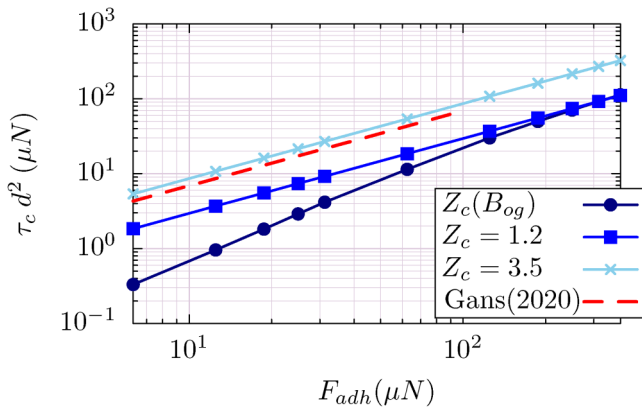


**FIG. 15.** Relation between the theoretical prediction of the macroscopic cohesive stress  $\tau_c d^2$  [Eq. (11)] and the contact adhesive force  $F_{adh}$  for different values of the density of cohesive contacts  $Z_c$ . The dashed line shows the prediction for the experimental data from Gans *et al.* [15], together with the corresponding range of values.

Figure 15 is a good illustration of the way the relation between macroscopic stress and contact adhesion is very dependent on the details of the cohesive texture and the way it is estimated. It also shows that the numerical cohesive matter simulated here behaves very similarly to the experimental cohesion-controlled material of Gans *et al.* [15] in terms of the dependance  $\tau_c \propto F_c$ .

However, Gans *et al.* [15], as we did, assume a constant coefficient  $\mu$ . A constant volume fraction  $\phi$  and a constant density of cohesive contacts are also chosen. The latter are, however, very dependent on the system cohesion [24,25]. Hence, Fig. 15 and the linearity of the relation  $\tau_c \propto F_c/d$  do not give information on the dependence of  $\tau_c$  on the internal friction.

If the material obeys ideal Coulomb behavior, the stress state satisfies  $\tau = \mu\sigma_n + \tau_c$ . If  $\tau_c = \mu\sigma_c$ , then  $\mu = \tau/(\sigma_n - \sigma_c)$ , and an increase of the contact adhesion and of  $\sigma_c$  may coincide with an increase of  $\mu$ . If we do not assume  $\tau_c = \mu\sigma_c$ , we have  $\mu = (\tau - \tau_c)/\sigma_n$ , and an increase of the contact adhesion and of  $\tau_c$  may coincide with a decrease of  $\mu$ .

This is what is observed in Iordanoff *et al.* [26], although the apparent friction (and not the Coulombic friction) is considered. Another difference is that [26] considers much smaller values of the reduced pressure  $P^*$  (about 10 times smaller), i.e., much stronger adhesive forces. Iordanoff *et al.* [26] attribute the decrease of friction with adhesion to the thinning of the shear zone where grains are irreversibly deformed. In that sense, their observation bears analogy with the scenario proposed in the present paper (Sec. V), invoking a failure plane resembling more and more solid-solid sliding interfaces when contact adhesion increases and resembling less and less collection of erratically colliding particles dissipating energy.

## VII. DISCUSSION

Simulation of the failure of cohesive granular steps, with varying intensities of the contact adhesive force, is presented. Failures are characterized through careful analysis of the grain displacement, which allows for deriving a chronology of the failure events. Focusing on the interface between moving and static materials, we infer the position of the failure plane, found to be compatible with a linear shape, in agreement with previous observations [34,36,40]. Plotting the failure orientation with the horizontal against the intensity of the contact adhesion, we disclose a nonmonotonous evolution.

Although the column collapse is intrinsically transient heterogeneous phenomena, it can be compared with experimental and numerical studies of wet shear flows [13,20], provided we adopt a definition of the reduced pressure relevant to the collapse configuration. Doing so, and computing the apparent friction coefficient, we observe consistent behaviors. The weak values of friction in our simulation point at the short-range of the contact adhesion model implemented here, which does not consider any debonding distance characteristic of capillary cohesion [20]. Our model nevertheless reproduces the behavior of sticky polymer-coated grains [15], in

particular, the dependence between the macroscopic cohesion and the contact adhesion and the range of friction explored.

Assuming that the material behaves as an ideal Coulomb material allows for writing the equilibrium of an edge of material at incipient failure, for which the failure angle is related to the internal frictional properties of the material. This provides an interpretation of the nonmonotonous behavior of the orientation of the failure plane. Although the systems studied here are past equilibrium and incipient failure, the nonmonotonous evolution of the failure orientation may hint at a cohesion-induced weakening mechanism, by which stronger contact adhesion involves weaker friction.

## ACKNOWLEDGMENT

The authors acknowledge a very fruitful reviewing process.

## AUTHOR DECLARATIONS

### Conflict of Interest

The authors have no conflicts to disclose.

## DATA AVAILABILITY

The data that support the findings of this study are available from the corresponding author upon reasonable request.

## REFERENCES

- [1] Jaeger, H. M., S. R. Nagel, and R. P. Behringer, “Granular solids, liquids, and gases,” *Rev. Mod. Phys.* **68**, 1259–1273 (1996).
- [2] Rumpf, H. C. H., “Zur Theorie der Zugfestigkeit von Agglomeraten bei Kraftübertragung an Kontaktpunkten,” *Chem. Ing. Tech.* **42**, 538–540 (1970).
- [3] Schubert, H., “Capillary forces—Modeling and application in particulate technology,” *Powder Technol.* **37**(1), 105–116 (1984).
- [4] Jenike, A. W., “A theory of flow of particulate solids in converging and diverging channels based on a conical yield function,” *Powder Technol.* **50**, 229–236 (1987).
- [5] Pierrat, P., D. K. Agrawal, and H. S. Caram, “Effect of moisture on yield locus of granular materials: Theory of shift,” *Powder Technol.* **99**, 220–227 (1998).
- [6] Klausner, J. F., D. Chen, and R. Mei, “Experimental investigation of cohesive powder rheology,” *Powder Technol.* **112**(1–2), 94–101 (2000).
- [7] Muzzio, F. J., C. L. Goodridge, A. Alexander, P. Arratia, H. Yang, O. Sudah, and G. Mergen, “Sampling and characterization of pharmaceutical powders and granular blends,” *Int. J. Pharm.* **250**(1), 51–64 (2003).
- [8] Emery, E., J. Oliver, T. Pugsley, J. Sharma, and J. Zhou, “Flowability of moist pharmaceutical powders,” *Powder Technol.* **189**(3), 409–415 (2009).
- [9] Lumay, G., F. Boschini, K. Traina, S. Bontempi, J.-C. Remy, R. Cloots, and N. Vandewalle, “Measuring the flowing properties of powders and grains,” *Powder Technol.* **224**, 19–27 (2012).
- [10] Liu, Z., Q. Li, and J. Zhang, “Effect of moisture content on flow behavior and resistance characteristics of dense-phase pneumatic conveying,” *Powder Technol.* **387**, 1–8 (2021).
- [11] Richefeu, V., M. S. El Youssoufi, and F. Radjai, “Shear strength properties of wet granular materials,” *Phys. Rev. E* **73**(5), 051304 (2006).
- [12] Badetti, M., A. Fall, F. Chevoir, and J.-N. Roux, “Shear strength of wet granular materials: Macroscopic cohesion and effective stress,” *Eur. Phys. J. E* **41**, 68 (2018).
- [13] Badetti, M., A. Fall, D. Hautemayou, F. Chevoir, P. Aïmedieu, S. Rodts, and J.-N. Roux, “Rheology and microstructure of unsaturated wet granular materials: Experiments and simulations,” *J. Rheol.* **62**, 1175–1196 (2018).
- [14] Deboeuf, S., and A. Fall, “Cohesion and aggregates in unsaturated wet granular flows down a rough incline,” *J. Rheol.* **67**(4), 909 (2023).
- [15] Gans, A., O. Pouliquen, and M. Nicolas, “Cohesion-controlled granular material,” *Phys. Rev. E* **101**, 032904 (2020).
- [16] Mandal, S., M. Nicolas, and O. Pouliquen, “Insights into the rheology of cohesive granular media,” *Proc. Natl. Acad. Sci. U.S.A.* **117**, 8366–8373 (2020).
- [17] Radjai, F., and V. Richefeu, “Contact dynamics as a nonsmooth discrete element method,” *Mech. Mater.* **41**, 715–728 (2009).
- [18] Staron, L., and A. Abramian, “Time steps vs cohesion in non-smooth contact dynamics algorithm,” in Proceedings of the 14th World Congress on Computational Mechanics (WCCM) ECCOMAS Congress 2020, Paris, France, 19–24 July 2020.
- [19] Berger, N., E. Azéma, J.-F. Douce, and F. Radjai, “Scaling behaviour of cohesive granular flows,” *Europhys. Lett.* **112**(6), 64004 (2015).
- [20] Khamseh, S., J.-N. Roux, and F. Chevoir, “Flow of wet granular materials: A numerical study,” *Phys. Rev. E* **92**, 022201 (2015).
- [21] Vo, T. T., S. Nezamabadi, P. Mutabaruka, J.-Y. Delenne, and F. Radjai, “Additive rheology of complex granular flows,” *Nat. Commun.* **11**(1), 1476 (2020).
- [22] Vo, T. T., P. Mutabaruka, S. Nezamabadi, J.-Y. Delenne, and F. Radjai, “Evolution of wet agglomerates inside inertial shear flow of dry granular materials,” *Phys. Rev. E* **101**(3), 032906 (2020).
- [23] Abramian, A., L. Staron, and P. Y. Lagrée, “The slumping of a cohesive granular column: Continuum and discrete modelling,” *J. Rheol.* **64**, 1227–1235 (2020).
- [24] Rognon, P. G., J.-N. Roux, M. Naaïm, and F. Chevoir, “Dense flows of cohesive granular materials,” *J. Fluid Mech.* **596**, 21–47 (2008).
- [25] Du Than, V., S. Khamseh, A. Minh Tang, J.-M. Pereira, F. Chevoir, and J.-N. Roux, “Basic mechanical properties of wet granular materials: A DEM study,” *J. Eng. Mech. Am. Soc. Civil Eng.* **143**(1), C4016001 (2017).
- [26] Iordanoff, I., N. Fillot, and Y. Berthier, “Numerical study of a thin layer of cohesive particles under plane shearing,” *Powder Technol.* **159**(1), 46–54 (2005).
- [27] Mériaux, C., and T. Triantafyllou, “Scaling the final deposits of dry cohesive granular columns after collapse and quasi-static fall,” *Phys. Fluids* **20**(3), 033301 (2008).
- [28] Artoni, R., A. C. Santomaso, F. Gabrieli, D. Tono, and S. Cola, “Collapse of quasi-two-dimensional wet granular columns,” *Phys. Rev. E* **87**(3), 032205 (2013).
- [29] Claudio Santomaso, A., S. Volpato, and F. Gabrieli, “Collapse and runout of granular columns in pendular state,” *Phys. Fluids* **30**(6), 063301 (2018).
- [30] Bougouin, A., L. Lacaze, and T. Bonometti, “Collapse of a liquid-saturated granular column on a horizontal plane,” *Phys. Rev. Fluids* **4**(12), 124306 (2019).
- [31] Li, P., D. Wang, Y. Wu, and Z. Niu, “Experimental study on the collapse of wet granular column in the pendular state,” *Powder Technol.* **393**, 357–367 (2021).
- [32] Abramian, A., P. Y. Lagrée, and L. Staron, “How cohesion controls the roughness of a granular deposit,” *Soft Matter* **17**(47), 10723–10729 (2021).

- [33] Heyman, J., “The stability of a vertical cut,” *Int. J. Mech. Sci.* **15**(10), 845–854 (1973).
- [34] Gans, A., A. Abramian, P.-L. Lagrée, M. Gong, A. Sauret, O. Pouliquen, and M. Nicolas, “Collapse of a cohesive granular column,” *J. Fluid Mech.* **959**, A41 (2023).
- [35] Kadau, D., G. Bartels, and L. D. E. Wolf Brendel, “Contact dynamics simulations of compacting cohesive granular systems,” *Comput. Phys. Commun.* **147**, 190–193 (2002).
- [36] Staron, L., A. Abramian, and P.-Y. Lagrée, “Capturing the failure of a cohesive granular step,” *EPJ Web Conf.* **249**, 08006 (2021).
- [37] Nase, S. T., W. L. Vargas, A. A. Abatan, and J. McCarthy, “Discrete characterization tools for cohesive granular material,” *Powder Technol.* **116**, 214–223 (2001).
- [38] Martín, C. M., “The use of adaptive finite-element limit analysis to reveal slip-line fields,” *Géotech. Lett.* **1**(2), 23–29 (2011).
- [39] Mandal, S., M. Nicolas, and O. Pouliquen, “Rheology of cohesive granular media: Shear banding, hysteresis, and nonlocal effects,” *Phys. Rev. X* **11**(2), 021017 (2021).
- [40] Gans, A., Rheology of cohesive powders: Experiments and modelisation, Ph.D. thesis, Aix-Marseille University, Marseille, 2021).
- [41] Courrech du Pont, S., P. Gondret, B. Perrin, and M. Rabaud, “Granular avalanches in fluids,” *Phys. Rev. Lett.* **90**(4), 044301 (2003).
- [42] GDR MiDi, “On dense granular flows,” *Eur. Phys. J. E* **14**, 341–365 (2004).
- [43] Nedderman, R. M., *Statics and Kinematics of Granular Materials* (Cambridge University Press, Cambridge, 1992).
- [44] Restagno, F., L. Bocquet, and E. Charlaix, “Where does a cohesive granular heap break,” *Eur. Phys. J. E* **14**, 177–183 (2004).
- [45] Ma, F., L. Duchemin, P.-Y. Lagrée, and L. Staron, “Failure of a cohesive granular column” (unpublished).